

## Article

# The Applications of WFEM in the Exploration of Medium-Depth Geothermal Resources

Guoqiang Fu <sup>1</sup>, Zhuqiang Li <sup>1,2,\*</sup> , Qiangjiang Zhang <sup>3,4,5,\*</sup>, Tao Guo <sup>2</sup>, Qiyun Jiang <sup>3,5</sup>, Yonghong Yang <sup>2</sup>, Xueguo Chen <sup>2</sup>, Chuang Lei <sup>6</sup> and Jie Li <sup>4,7</sup>

<sup>1</sup> School of Resources and Geosciences, China University of Mining and Technology, Xuzhou 221116, China; gq\_jybf@cumt.edu.cn

<sup>2</sup> Exploration and Development Research Institute, Shengli Oilfield Company, SINOPEC, Dongying 257000, China

<sup>3</sup> Institute of Urban Underground Space and Energy Studies, The Chinese University of Hong Kong (Shenzhen), Shenzhen 518172, China

<sup>4</sup> College of Earth Sciences, Guilin University of Technology, Guilin 541006, China

<sup>5</sup> Institute of Green and Low-Carbon Energy Science and Technology in Chongqing, Chongqing 402160, China

<sup>6</sup> Sinopec Geophysical Corporation Geographical & Geological Exploration Branch, Wuhan 430073, China

<sup>7</sup> The Guangxi Key Laboratory of Theory and Technology for Environmental Pollution Control, Guilin 541006, China

\* Correspondence: lizhuqiang.slyt@sinopec.com (Z.L.); qjz2018@glut.edu.cn (Q.Z.)

**Abstract:** Medium-depth geothermal energy mainly consists of two types, hydrothermal and dry-heat rock. With huge resource reserves, its exploration and development are of great significance to the transformation of China's energy structure and the realization of the goal of "Double-Carbon". From the differences in the electrical characteristics between hydrothermal and hot dry rock geothermal resources, this project uses the numerical modeling of the wide field electromagnetic (WFEM) method as a tool to design a model of typical geothermal resources. Then, we summarize and analyze the detection capability of the WFEM by calculating the WFEM response under the conditions of different depths, resistivity values, thickness-to-depth ratios and other parameters. Moreover, aiming at the key problems faced by the WFEM in real applications, we discuss the factors affecting the detection accuracy and give solutions to improve the reliability of the detection results. Finally, the medium-depth geothermal energy detection in the Jiyang Depression of Shandong is presented as an example, showing how the WFEM detection technique was used with the inversion result profile obtained. By comparing the results of geomagnetic and seismic detection on the same survey line, it is demonstrated that the WFEM method has great potential in the exploration of medium-depth geothermal energy and can be the preferred method.

**Keywords:** wide field electromagnetic; geothermal energy; Jiyang Depression; geothermal exploration



**Citation:** Fu, G.; Li, Z.; Zhang, Q.; Guo, T.; Jiang, Q.; Yang, Y.; Chen, X.; Lei, C.; Li, J. The Applications of WFEM in the Exploration of Medium-Depth Geothermal Resources. *Energies* **2024**, *17*, 1904. <https://doi.org/10.3390/en17081904>

Academic Editors: Davide Di Battista, Fabio Fatigati and Marco Di Bartolomeo

Received: 12 March 2024

Revised: 13 April 2024

Accepted: 13 April 2024

Published: 17 April 2024



**Copyright:** © 2024 by the authors. Licensee MDPI, Basel, Switzerland. This article is an open access article distributed under the terms and conditions of the Creative Commons Attribution (CC BY) license (<https://creativecommons.org/licenses/by/4.0/>).

## 1. Introduction

Geothermal energy is abundant and has low operating costs. It is the only renewable and clean energy extracted from the Earth's resources that is not affected by weather conditions and seasonal changes [1,2]. Geothermal energy is divided into (Figure 1): shallow geothermal energy (depth less than 200 m), hydrothermal geothermal energy (depth 200~3000 m) and hot dry rock geothermal energy (depth 3~10 km) [3]. The latest research shows that hydrothermal geothermal and hot dry rock geothermal are "symbiotic" [4]. Most of the hot dry rock geothermal systems that have been exposed are impermeable high-temperature rock formations on the wings of specific hydrothermal types or contain a small amount of steam, except for the high-temperature geothermal systems controlled by volcanic activity or magma waste heat that have clear evidence of volcanic activity or magma waste heat in some areas in China. The symbiotic characteristics of hot dry rock geothermal

systems and hydrothermal geothermal systems are very obvious in high-temperature rock formations [4,5].

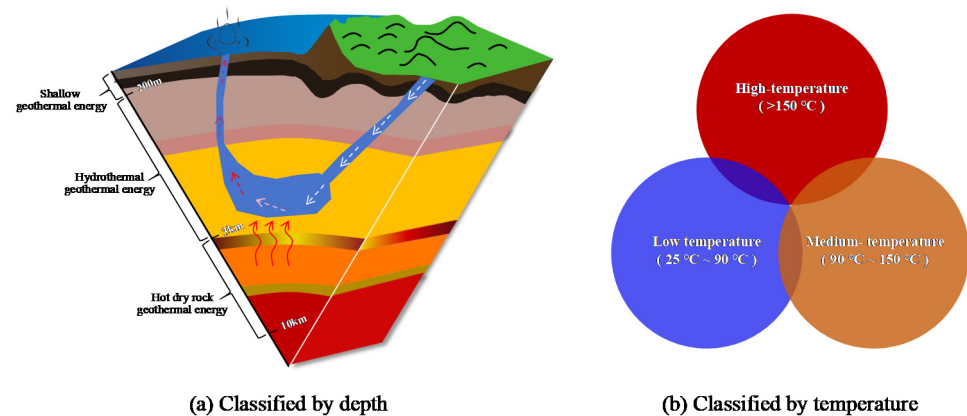


**Figure 1.** The classification of the geothermal energy resource.

To distinguish “geothermal resources”, the mid-deep geothermal resources are classified as the hydrothermal type and dry hot rock type [4,6]. Correspondingly, the exploration and development of mid-deep geothermal energy can be divided into two types: traditional hydrothermal geothermal systems and enhanced geothermal systems. Traditional hydrothermal geothermal resources mainly exist in highly permeable pores or fissure media in the form of liquid water or steam [7]. According to the different geological elements and geological process characteristics, they can be divided into two types: namely, the magma type distributed at the active edge of the plate or volcanic active area within the plate and with melt/magma pockets as the main heat source, the faults-deep circulation type closely related to regional deep faults, and the fault basin type related to higher heat flow background in the extension zone or low heat flow background in the stable zone [8]. The dry hot rock geothermal resources are huge. It is estimated that the total geothermal energy resources located 3–10 km underground in the globe are about  $4.95 \times 10^{15}$  t standard coal, which is equivalent to 30 times the energy contained in all the coal, oil and natural gas in the world.

The geothermal energy industry is chained with three main links: namely, resource detection, drilling and mining and comprehensive utilization [9]. The detection of geothermal energy is an upstream industry, the first link in the chain. According to surveys, Tibet, western Yunnan and western Sichuan are the three regions with the richest high-temperature geothermal resources in China which can meet the requirements for large-scale industrial power generation. The methods for the detection of mid-deep geothermal energy mainly include electromagnetic methods, seismic methods and gravity. Among them, the electromagnetic methods include magnetotelluric methods (MT, AMT) [10–15] and time-frequency electromagnetic methods (TFEM) [16], the controlled source audio electromagnetic method (CSAMT) [17–19] and the wide field electromagnetic method (WFEM) [20,21]. Seismic methods mainly include reflection seismic and micro-motion methods [22–24]. The main role of gravimetry in mid-deep geothermal detection is to extract geological information related to basement undulations, hidden faults and local structures, etc., to reflect the regional structures and to locate the favorable areas for heat storage [25–27]. In recent years, the electromagnetic method has become the preferred method for mid-deep geothermal exploration due to its advantages in detection accuracy and construction cost. Taking the geothermal resource exploration of Yueliang Bay in Binhai County, Jiangsu Province as an example, three methods including CSAMT, WFEM and micro-motion detection were applied for comparative verification. The strata are divided according to the detection results of the three methods and the inferred fault structures are basically consistent. After drilling by DR01, the borehole verification is highly consistent, confirming the effectiveness of the comprehensive geophysical method and technology. It also shows that the WFEM

method can effectively suppress interference while ensuring the exploration depth. This method has such obvious advantages that it can be, therefore, taken as the preferred method for geothermal resource exploration [18].

The main problems in the exploration of mid-deep geothermal energy include serious human interference, large detection depth, poor terrain conditions and complex geological structures, making geophysical detection difficult. The conventional electromagnetic method has a relatively low accuracy when the detection depth is met, so it is difficult to form an effective trap for mid-deep geothermal resource targets. The WFEM method is a large-depth and high-precision artificial source frequency domain electromagnetic method proposed by the Academician He Jishan [28]. It has three major advantages: large depth of detection, high precision and strong anti-interference ability. It has been applied in many domestic geothermal exploration projects in China and has been recognized as the major geophysical method for the exploration of deep geothermal resources [21].

Based on the WFEM method, a theoretical model is designed according to the electrical characteristics of the mid-deep hydrothermal geothermal and hot dry rock geothermal resources, and the detection capabilities of the WFEM method are analyzed. These analyses contribute to enhancing the understanding of utilizing the WFEM method for geothermal energy resource exploration, offering theoretical support for the practical cases discussed in subsequent sections. Then, we discuss and analyze the key issues in the WFEM observation system design, data processing and inversion imaging in mid-deep geothermal energy detection. Finally, the processing methods and solutions to key issues in WFEM detection are discussed through the case of mid-deep geothermal energy potential evaluation and detection in Jiyang, Jinan City. Through the comprehensive analysis of existing seismic profiles, the WFEM method provides an important theoretical basis for the high-precision detection of mid-deep geothermal energy.

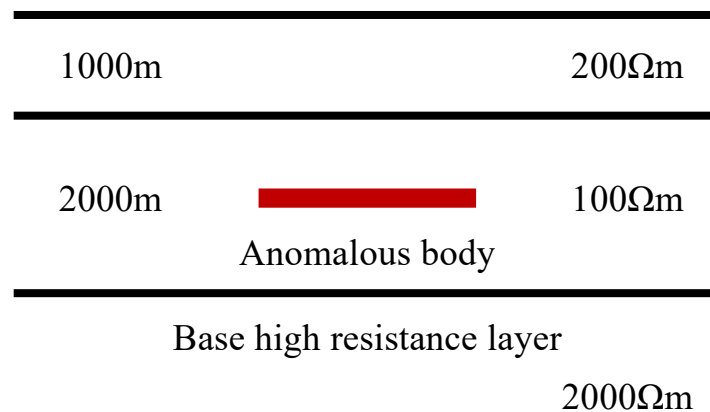
## 2. Analysis of the Detection Capability of WFEM for Medium and Deep Targets

### 2.1. Analysis of the Detection Capabilities of Hydrothermal Geothermal Resources

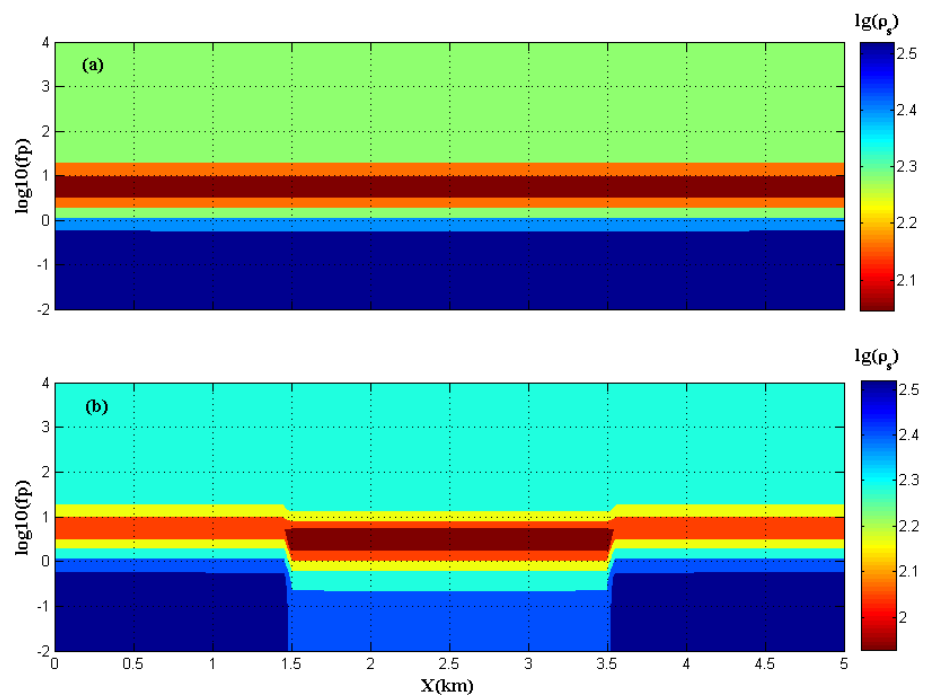
The design of the three-layer H-shaped geoelectric model is shown in Figure 2 (taking into account the stratigraphic structure in the case of Jiyang geothermal detection in this paper). The resistivity values of the first, second and third layers are 200  $\Omega\text{m}$ , 100  $\Omega\text{m}$  and 2000  $\Omega\text{m}$ , respectively. The thicknesses of the first and second layers are 1000 m and 2000 m, respectively. The hydrothermal geothermal target body exhibits low resistance characteristics; the depth of the top interface is 2000 m, and the initial resistivity is set to 10  $\Omega\text{m}$ . We design the hydrothermal geothermal targets with different thicknesses and different electrical properties, and use the 1D WFEM method to carry out numerical simulation research and summarize and analyze the detection capabilities of the WFEM method for mid-deep hydrothermal geothermal targets. In the numerical modeling, an equatorial device is used with the coordinates of point A of the long wire source being (2 km, -12 km, 0), respectively, and the coordinates of point B being (3 km, -12 km, 0), respectively. The wire length is 1 km and the distance between transmitting and receiving is 12 km. There are a total of 61 transmitting frequencies, with the highest frequency being 10 kHz, while the lowest frequency is 0.01 Hz evenly distributed on the logarithmic interval.

Figure 3 gives the numerical modeling results in which Figure 3a shows the wide field apparent resistivity profile without a hydrothermal target. Figure 3b shows the wide field apparent resistivity profile after placing a target body with a thickness of 100 m (a thickness-to-depth ratio of about 5%), a width of 2000 m and a resistivity of 10  $\Omega\text{m}$ .

It can be seen from Figure 3 that the wide field apparent resistivity has obvious anomaly characteristics when the second layer of the H-type geoelectric model contains a low-resistance hydrothermal geothermal target body. The amplitude of the apparent resistivity anomaly corresponding to the target body is 23.4% (from 111  $\Omega\text{m}$  to 85  $\Omega\text{m}$ ), while the measurement accuracy of the WFEM method measured data is 5%.



**Figure 2.** Schematic diagram of three-layer H-shaped geoelectric model.



**Figure 3.** Apparent resistivity profile using WFEM method. (a) No anomaly body (b) there is an anomaly body.

In order to study the detection ability of the WFEM method on hydrothermal geothermal targets, on the basis of the above modeling examples, we change the resistivity, thickness and depth parameters of the targets, and then summarize and analyze the results of the numerical simulation to draw regular conclusions.

Figure 4 shows the overlay of the curves of the measuring points (2.5 km, 0 m, 0 m) changing with frequency at different resistivity parameters of the target body with a thickness-to-depth ratio of 5%. It can be seen that the abnormal amplitude of the wide field apparent resistivity caused by the target body becomes larger as the resistivity value of the target body decreases (from 50 Ωm to 1 Ωm). Compared with the background model, the maximum abnormal amplitudes are 4.5%, 13.2%, 23.4%, 39.6%, 64.0% and 78.4%, respectively. Taking 5% as the amplitude of the anomaly as the identification limit for low-resistance anomalies deeper than 2000 m, when the thickness-to-depth ratio is 5%, the difference in resistivity can be detected when it is a difference of more than two times (when the resistivity of background is 100 Ωm, the low-resistance anomaly targets that can be detected have a volume resistivity value slightly less than 50 Ωm).

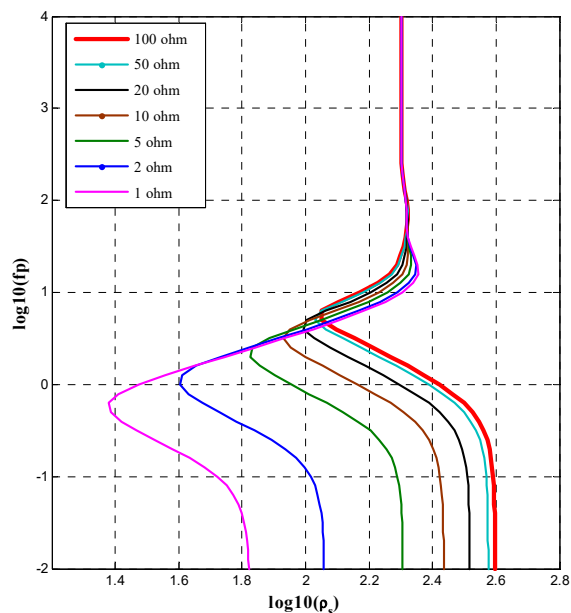


**Figure 4.** Overlay of wide field apparent resistivity curves with different resistivity parameters (5% thickness-to-depth ratio).

Table 1 exhibits the numerical results of the wide field apparent resistivity anomaly amplitude when the hydrothermal geothermal target body has different depths, thickness-to-burial ratios and resistivity parameters. The resistivity values of the layer background are 100 Ωm and 200 Ωm, respectively, when the depths of the target’s top interface are located at 2000 m and 500 m, respectively. Taking 5% as the abnormal amplitude and as the identification limit, it can be seen that when the thickness and depth ratios of the low-resistance target body are 1%, 2%, and 5%, respectively, the difference in resistivity between the target body and the background surrounding rock is greater than 10, 5, 2 times, showing that it is detectable. This can be summarized as a general conclusion on the ability of the WFEM method to detect mid-deep geothermal resources.

**Table 1.** Numerical modeling results of the hydrothermal geothermal target body with different parameters (“/” indicates not simulated, The same as below).

Depth of Target (m)	Thickness to Depth Ratio	Numerical Modeling Results							
		Resistivity (Ωm)	100	50	20	10	5	2	1
2000	5%	Resistivity (Ωm)	100	50	20	10	5	2	1
		Maximum abnormal amplitude (%)	/	4.5	13.2	23.4	39.6	64.0	78.4
		Explorability(Yes or No)	/	N	Y	Y	Y	Y	Y
	2%	Resistivity (Ωm)	100	50	20	10	5	2	1
		Maximum abnormal amplitude (%)	/	1.0	5.3	9.3	18.3	36.9	54.5
		Explorability(Yes or No)	/	N	Y	Y	Y	Y	Y
	1%	Resistivity (Ωm)	100	50	20	10	5	2	1
		Maximum abnormal amplitude (%)	/	0.3	3.3	6.9	11.5	26.1	41.5
		Explorability(Yes or No)	/	N	N	Y	Y	Y	Y

Table 1. Cont.

Depth of Target (m)	Thickness to Depth Ratio	Numerical Modeling Results							
		Resistivity ( $\Omega\text{m}$ )	100	50	20	10	5	2	1
500	5%	Resistivity ( $\Omega\text{m}$ )	100	50	20	10	5	2	1
		Maximum abnormal amplitude (%)	2.7	8.1	24.7	51.9	100	179	215
		Explorability(Yes or No)	N	Y	Y	Y	Y	Y	Y
	2%	Resistivity ( $\Omega\text{m}$ )	100	50	20	10	5	2	1
		Maximum abnormal amplitude (%)	1.4	4.1	12.4	26.5	54.3	123	184
		Explorability(Yes or No)	N	N	Y	Y	Y	Y	Y
	1%	Resistivity ( $\Omega\text{m}$ )	100	50	20	10	5	2	1
		Maximum abnormal amplitude (%)	0.92	2.7	8.3	17.7	36.5	89.3	152
		Explorability(Yes or No)	N	N	Y	Y	Y	Y	Y

## 2.2. Analysis of the Detection Capabilities of Hot Dry Rock Geothermal Resources

Figure 5 shows the model of a hot dry rock geothermal resource. The resistivity values of the first, second and third layers are 200  $\Omega\text{m}$ , 100  $\Omega\text{m}$  and 10,000  $\Omega\text{m}$ , respectively. The thicknesses of the first and second layers are 1000 m and 3000 m, respectively. The hot dry rock geothermal target body exhibits high resistance characteristics, rising upward and protruding into the second layer of rock. The top interface is at a depth of 3000 m (hot dry rock is usually at a depth of 3–10 km) and the initial resistivity is set to 100  $\Omega\text{m}$ . We design hot dry rock geothermal resource targets with different thicknesses and different electrical properties, use the 1D WFEM method to carry out numerical simulation research and summarize and analyze the detection capabilities of the WFEM method for mid-deep hydrothermal geothermal targets. In the numerical modeling, an equatorial device is used with the coordinates of point A of the long wire source being (2 km, −16 km, 0), respectively, and the coordinates of point B being (3 km, −16 km, 0), respectively. The wire length is 1 km and the transmitting and receiving distance is 16 km. There are a total of 61 transmitting frequencies, with the highest frequency being 10 kHz and the lowest frequency 0.01 Hz being evenly distributed on the logarithmic interval.

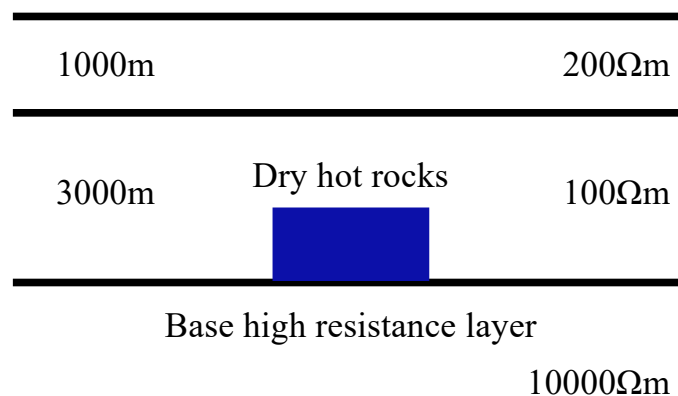
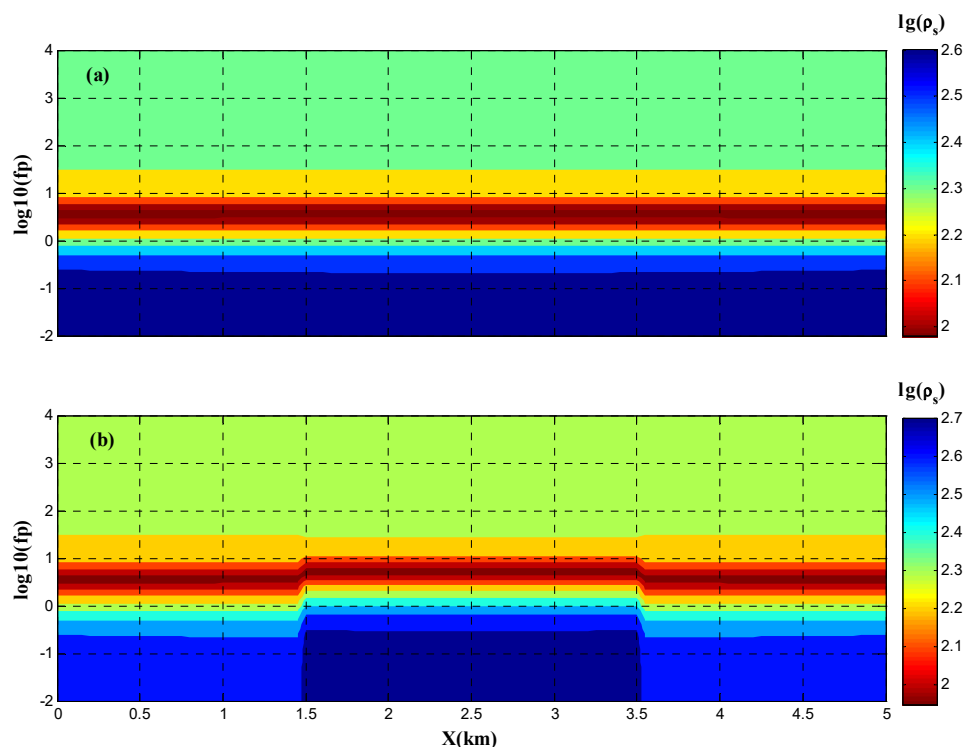


Figure 5. Schematic diagram of H-shaped model of hot dry rock mass.

Figure 6 gives the numerical modeling results, in which Figure 6a depicts the wide field apparent resistivity profile of the uninvaded hot dry rock target body. Figure 6b depicts the wide field apparent resistivity profile after intruding into a hot dry rock-type geothermal target body with a resistivity of 200  $\Omega\text{m}$ . The image indicates that the wide field apparent resistivity exhibits clear anomalous characteristics when a high-resistance hydrothermal

geothermal target body is present in the second layer of the H-type geoelectric model. The amplitude of the apparent resistivity anomaly corresponding to the target body is 26.5% (from 113.6  $\Omega\text{m}$  to 143.7  $\Omega\text{m}$ ).



**Figure 6.** Apparent resistivity profile using WFEM method (a) No hot dry rock target (b) There is hot dry rock target.

Table 2 exhibits the numerical results of the amplitude of the wide field apparent resistivity anomaly when the hot dry rock geothermal target body has different depths, thickness-to-burial ratios and resistivity parameters. The depths of the top interfaces of the invaded targets are 3000 m, 3500 m and 3800 m, respectively, and the resistivity values are 200  $\Omega\text{m}$ , 500  $\Omega\text{m}$ , 1000  $\Omega\text{m}$ , 2000  $\Omega\text{m}$ , 5000  $\Omega\text{m}$  and 10,000  $\Omega\text{m}$ , respectively. Taking 5% as the abnormal amplitude and as the identification limit, it is evident that when the thickness and depth ratio of the high-resistance target body is greater than 13.3% and 5.1%, respectively, the resistivity difference between the target body and the background surrounding rock is greater than 2.5 times, which is detectable. In addition, for high-resistance anomaly target objects, the amplitude of a wide field apparent resistivity anomaly changes little when the resistivity difference between the anomaly object and the background surrounding rock is greater than a certain value. This can be summarized as a general conclusion on the ability of the WFEM method to detect mid-deep hot dry rock geothermal resources.

**Table 2.** Numerical modeling results of different parameters of hot dry rock geothermal target body.

Depth of Target (m)	Thickness to Depth Ratio	Numerical Modeling Results							
		Resistivity ( $\Omega\text{m}$ )	100	200	500	1000	2000	5000	10,000
3000	28.5%	Maximum abnormal amplitude (%)	/	26.5	50.4	59.9	65.1	68.5	69.9
		Explorability	/	Y	Y	Y	Y	Y	Y

Table 2. Cont.

Depth of Target (m)	Thickness to Depth Ratio	Numerical Modeling Results							
		Resistivity ( $\Omega\text{m}$ )	100	200	500	1000	2000	5000	10,000
3500	13.3%	Resistivity ( $\Omega\text{m}$ )	100	200	500	1000	2000	5000	10,000
		Maximum abnormal amplitude (%)	/	11.3	19.8	23.0	24.7	25.7	26.2
		Explorability	/	Y	Y	Y	Y	Y	Y
3800	5.1%	Resistivity ( $\Omega\text{m}$ )	100	200	500	1000	2000	5000	10,000
		Maximum abnormal amplitude (%)	/	4.1	6.8	7.7	8.2	8.6	8.7
		Explorability	/	N	Y	Y	Y	Y	Y

### 3. Study of the Key Issues of WFEM in Detection of the Mid-Deep Geothermal Energy

To study the key issues of WFEM detection, we first need to clarify the problems in the detection itself, secondly, consider what difficulties we face in the detection of the mid-deep geothermal resources, and finally, how to avoid or solve these problems. This paper elaborates on the factors affecting the accuracy of WFEM detection and the difficulties faced by mid-deep geothermal energy detection and gives corresponding solutions to provide theoretical references for the application of WFEM.

#### 3.1. Factors Affecting the Accuracy of Wide Field Electromagnetic Detection

Referring to the relevant literature and combined with the experience in practice of the WFEM method, the factors that affect the accuracy of WFEM detection can be summarized into three categories: (1) Objective factors, including volume effect (it can increase frequency density and number of frequencies), side effects (they can help to optimize survey line design; make surface element observations, reduce line spacing and point spacing, and improve lateral resolution), underground factors such as complex structure and small resistivity differences (they can be modeled and constrainedly inverted according to existing reference materials to improve the extraction of weak abnormal signals from observation data); (2) errors in observation data, including WFEM field source layout, field measurement and terrain errors and other factors; (3) factors brought by processing algorithms, including data editing and filtering algorithms, static effect processing methods, inversion initial model selection and inversion methods and so on. Among the above three types of factors, the first one is an objective factor that is common in electromagnetic detection methods. The second and third ones are the key issues in WFEM detection, which can directly affect detection accuracy.

##### 3.1.1. Observation Data Error

There are three major factors affecting the errors in observation data:

###### (1) Field source deployment factors

In the WFEM method observation system, the field source deployment is a very important part that directly affects the magnitude of the signal strength of the measurement point, the signal-to-noise ratio quality of the observation data, and the magnitude of the field source effect [20,29,30]. In the field source layout, issues that need to be considered are as follows: the length of the AB wire, the difference in AB elevation, the field source grounding resistivity, the terrain difference and elevation difference between the field source and the measurement line, the electrical current between the field source and the measurement line complexity and the connection issues between multiple field sources.

In the cases of complex underground structures and poor terrain conditions, long measuring lines are usually connected by multiple field sources. Due to the influence of the field source effect, the wide field apparent resistivity of the measuring points at

the connection has a large difference (see the apparent resistivity curve of wide-area electromagnetic survey line field source connection in a certain area as shown in Figure 7, where the measuring point No. 170 is the dividing line). In the design process of long survey line observation systems, the electrical consistency of multiple field sources should be fully considered, and it must be ensured that multiple field sources are located on the same side of the survey line, or the areas should be considered with relatively simple electrical conditions between field sources and survey lines. In a field survey, the principle should be followed of finding the field source first and then adjusting the survey line according to the field source conditions, and the influence of the field source should be removed as much as possible during data processing.

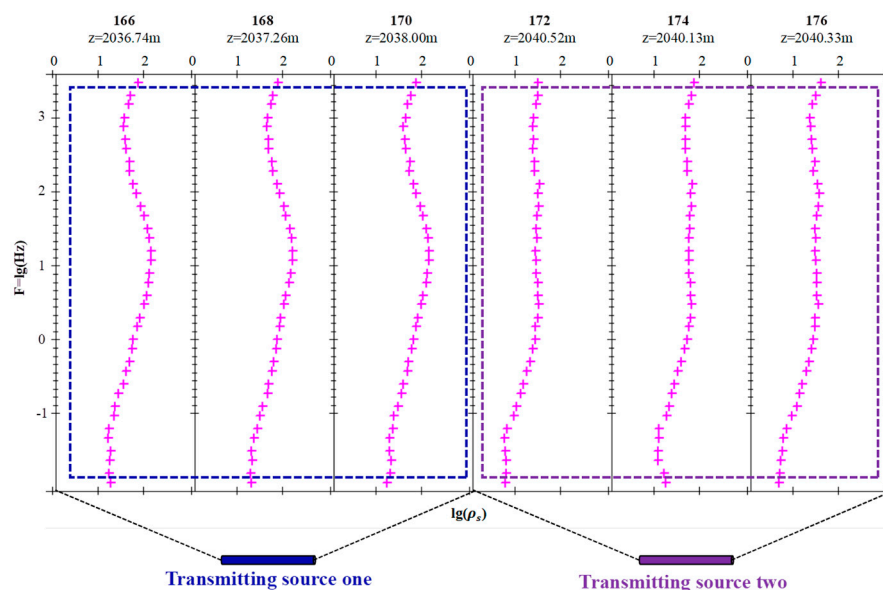


**Figure 7.** Apparent resistivity curve at the junction of multiple field sources of wide field electromagnetic survey lines in a certain area of Yunnan.

## (2) Measurement factors

The errors in the observation data mainly come from four aspects: no point position recorded at the measurement point MN, the MN angle deviation (as shown in Figure 8), the poor grounding effect of the MN and the wrong MN recording sequence. Among them, factors 1 and 4 are operational errors while factor 3 has a more mature solution and is usually not considered. The calculation method of wide field apparent resistivity based on any MN angle [31] can make the layout of field survey lines more flexible, but this requires consistent calculation of apparent resistivity in data processing. Currently, in WFEM 2D and 3D inversions, it is very difficult to obtain good imaging results. Therefore, we should try to ensure that MN and AB are parallel during data collection. Some measuring points can be translated if the layout conditions do not allow it.

## (3) Topographical factor

In recent years, terrain inversion can simulate terrain characteristics and effectively reduce the static effects caused by terrain and the problem of inaccurate target positioning. Due to factors such as the density of the model grid and the complexity of the terrain, there is always a deviation between the modeled terrain data and the actual terrain data which will have a greater impact on the imaging results at the medium-shallow level. Taking the 2D survey line as an example, the difference between the actual terrain and the model equivalent terrain is shown in Figure 9. When laying out survey lines, we should try to avoid terrain mutation areas and select relatively gentle areas to lay out survey points. In addition, we should try to increase the model grid density as much as possible to improve terrain accuracy.

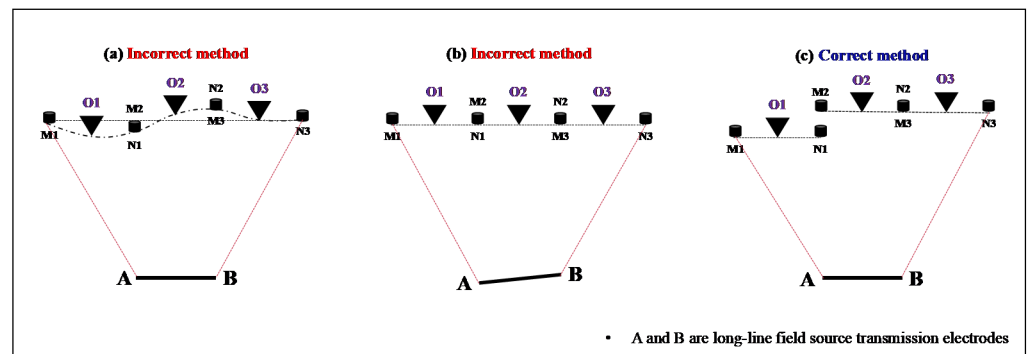


**Figure 8.** Schematic diagram of angle deviation (a) Measuring point angle deviation, (b) Field source angle deviation, (c) Measuring point translation.

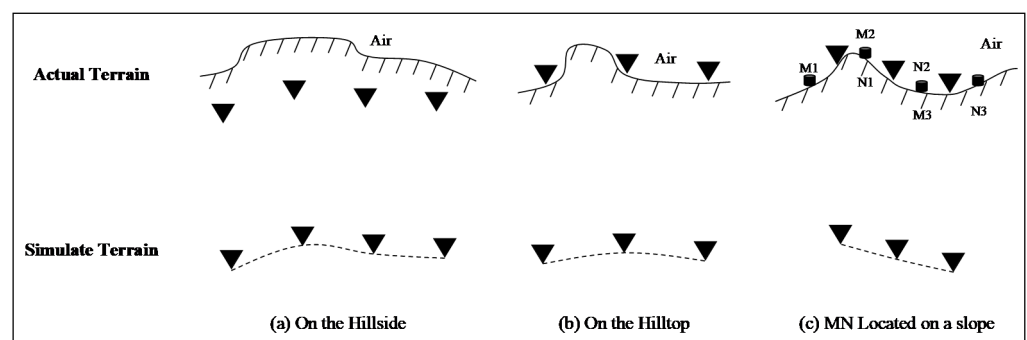


**Figure 9.** Schematic diagram of the difference between actual terrain and simulated terrain.

### 3.1.2. Processing algorithm factors

The factors of the processing algorithm mainly include four aspects:

#### (1) Data editing and filtering processing

In recent years, research on the data preprocessing of electromagnetic methods has gradually increased [32–34]. There are two opposite solutions in data preprocessing: (1) Using various algorithms to make the data smoother and consistent with the trend; (2) Keeping the glitches and small anomalies in the original data. The first solution is more reasonable overall and can ensure the stability of inversion convergence, but it also removes the weak local anomalies and reduces the ability to identify small structures. There are more abundant small structures and small anomalies in the inversion results of the second scheme, but its inversion convergence is poor and its inversion results are not smooth enough. Combining the two solutions, data preprocessing and editing may make the original data better, but at the same time, it may lead to deviating from reality and causing false anomalies. During the processing process, the processing results of other geophysical methods, geological structures, physical property data and drilling data, etc., are comprehensively considered from the overall trend to ensure that there are no deviations in large structures, and then weak abnormal signals are extracted through algorithms to improve the resolution of detection results.

#### (2) Static effect problem

The static effect refers to the phenomenon that the shape of the sounding curve remains unchanged due to local inhomogeneities in the shallow part of the measuring point, but an overall rise or fall occurs. The performance is particularly obvious in the areas with complex terrain conditions. Figure 10 shows the wide field electromagnetic apparent resistivity profile of Shangyun Coal Mine in Pu'er, Yunnan. When  $MN = 2$  m, a relatively serious static effect is produced due to the uneven surface (cracks). When  $MN = 8$  m, the impact of static effects is greatly reduced. The increase in  $MN$  spacing is equivalent to physically performing lateral filtering. For the areas with large terrain undulations or

serious shallow surface unevenness, solutions include, therefore, appropriately increasing the MN spacing, using mathematical algorithms to process raw data and using high-dimensional imaging algorithms.

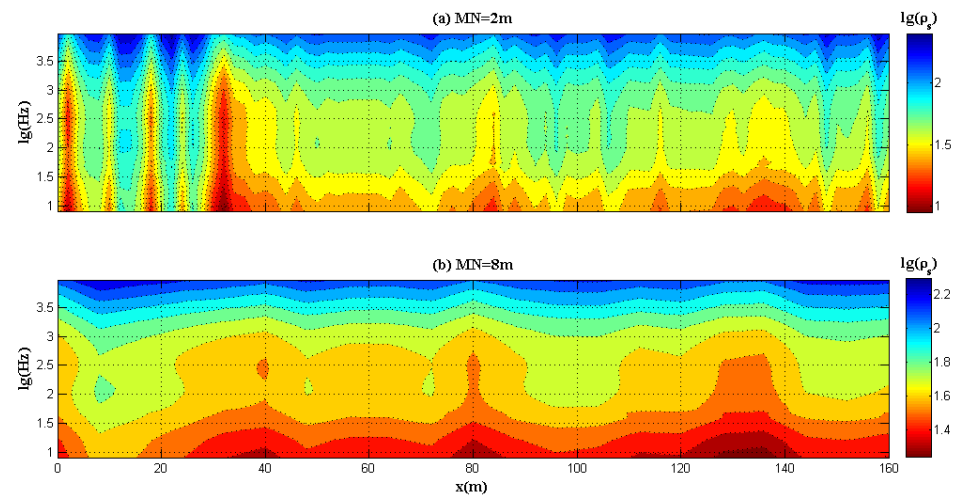


**Figure 10.** WFEM apparent resistivity profile of Pu'er Shangyun Coal Mine (a) MN = 2 m, (b) MN = 8 m.

### (3) Inversion of the initial model problem

In the regularized inversion algorithm, the initial model is crucial to the reliability of the inversion results [13,35,36]. Currently, two processing schemes are mainly applied: (1) Using low-dimensional inversion results as the initial model for high-dimensional inversion; (2) Using the uniform half-space model as the initial model. The first one is a commonly used solution in early inversion imaging algorithms. It has the advantages of faster convergence and obvious protrusion of the deep basement. The disadvantage is that it is easily affected by local minima and static effects, resulting in false anomalies. In addition, the high-dimensional inversion algorithm can greatly reduce the influence of local static effects; the use of 1D inversion results in the initial model requiring the separate processing of the original data. The second method has often been used in recent years. It has the advantages of good convergence and high reliability of mid-shallow-layer inversion results (fewer false anomalies), but the disadvantage is that the deep basement inversion effect is not obvious.

### (4) Problems with the inversion method

Theoretically, the WFEM method belongs to the artificial source electromagnetic method, and its imaging results using the source inversion algorithm are more reliable. In practice it is, however, very difficult to use the source inversion algorithm due to the influence of the coverage of the measurement points, the electrical unevenness between the field source and the measurement line, and the terrain effect (see the diagram of the layout of WFEM survey line in Lancang County, Pu'er City as shown in Figure 11): (1) AB is not at the same height as the survey line, and the terrain between the field source and the survey line is greatly undulating. When 1D and 2D source inversions are performed, the field source needs to be projected to the same altitude as the survey line and it is assumed that the electrical properties between the field source and the measurement line are uniform, which is quite different from the real situation. (2) In 3D exploration, it is necessary to arrange measuring points between the field source and the survey line. By inverting the electrical distribution under the measuring points, the accuracy of the forward data of the model in the inversion fitting can be improved, and the error of the inversion results with the source can be improved. It is related to the underground electrical distribution, and the error increases as the uneven electrical distribution increases.

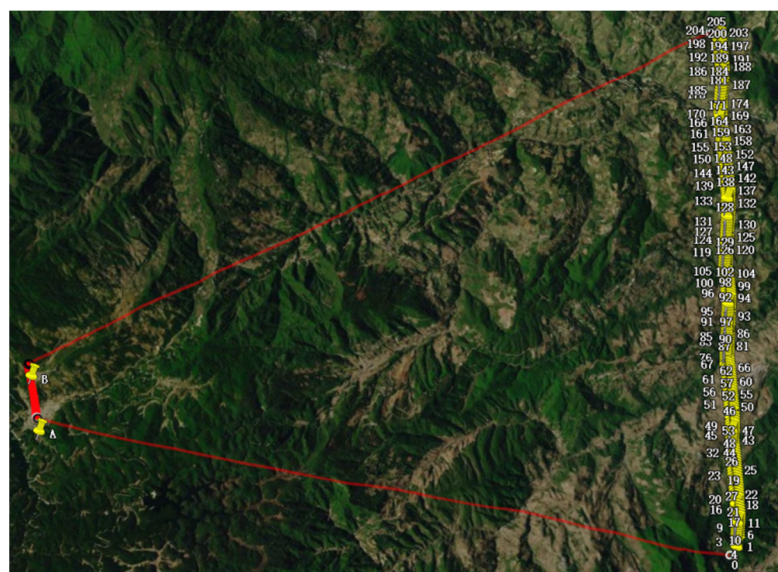


**Figure 11.** Layout of wide-area electromagnetic survey lines in Lancang County, Yunnan (A and B are long-line source electrodes in geophysical field operations).

The measures taken in processing the measured data of the WFEM method include field source correction; increasing the transmitting and receiving distance from the previous three times to the current 5–10 times the exploration depth; using wireless technology for the work areas with large terrain undulations and serious electrical non-uniformity, and source inversion algorithm. An active inversion algorithm should be used for the work areas with flat ground and relatively uniform electrical properties.

### 3.2. Difficulties Encountered by WFEM Method in the Detection of the Mid-Deep Geothermal Energy

The main problems faced by mid-deep geothermal energy detection include serious human interference, large detection depth, poor terrain conditions and complex geological structures, making geophysical detection difficult. Taking the three major high-temperature geothermal favorable areas of Tibet, western Yunnan and western Sichuan as examples, the specific problems faced are: (1) The terrain is complex, the jungle coverage is high and the data collection is difficult. The phenomenon of “noodles” in observation data is very serious and higher requirements are needed for data processing. (2) Field source deployment is more difficult with a larger field source effect due to the complexity of the terrain. In addition, due to a large detection depth and transmitter-transceiver distance, high-power transmitters (such as more than 200 kW) are required with greater transport difficulties on the third-class or fourth-class highways, making it impossible to transport field sources to reach the intended locations. (3) When the measurement line is too long, multiple field sources need to be connected. Due to the influence of topography and underground electrical inhomogeneity, the wide field apparent resistivity varies greatly at the connection of the measurement line, which creates issues for the processing and interpretation of the data. (4) In the interpretation, the determination of the lithology of hydrothermal geothermal targets needs to be supported by a combination of physical parameters such as polarisation rates and velocities. Besides, it is also necessary to grasp the mechanism of the heat source and the characteristics of the groundwater cycle, while the identification of hot dry rock bodies is more difficult so it is required to combine the geological and deep drilling data.

## 4. Case Analysis of the Evaluation of the Geothermal Energy Potential and the Detection of the Mid-Deep Layer of Jiyang Depression, Shandong Province

### 4.1. Geological and Geophysical Characteristics

#### 4.1.1. Tectonic Background

The Jiyang Depression is located in the southern part of the Bohai Bay basin, which is a superimposed fault basin of the middle and new Cenozoic era developed on the basis of the Paleozoic North China Stable Craton, with an extremely complicated internal structure. The Jiyang Depression is a first-level negative structural unit in the Bohai Bay Basin that converges to the west and spreads out to the east, held by the Puning Uplift and the Luxi Uplift. It is a part of the Bohai Bay Complex Block Basin. The Jiyang Depression is bounded by the Chengning Uplift to the north, the Luxi Uplift to the south, the Linqing Depression to the west and the Bozhong Depression to the east. The Cenozoic shows a NEE (near EW)-trending convex and concave structural pattern. It consists of the four depressions of Dongying, Huimin, Zhanhua and Chezhen and the Chengzikou uplift–Qingyun uplift, Yihezhuang uplift–Wudi uplift–Ningjin uplift, Chenjiazhuang uplift–Binxian uplift, Qingcheng uplift–Guangrao uplift, and the depression (sag) has a half-graben structure that is “broken in the north and overlapping in the south, deep in the north and shallow in the south”. From the perspective of the regional structure, the Wangpan Town industry region is located in the southwest of the Jiyang Depression and involves secondary structural units such as the Huimin Depression, Qingcheng Low Uplift, Linfanjia Low Uplift and Chezhen Depression (Figure 12).



**Figure 12.** Structural location map of Jiyang Depression [37].

#### 4.1.2. Characteristics of the Geothermal Field

The results of the geothermal gradient calculations show that the current average geothermal gradient in the Jiyang Depression is 35.5 °C/km, which is larger than the global average (30.0 °C/km) whereas the neighboring Bohai Basin has a geothermal gradient (33.0 °C/km) [38,39], which is close to the overall average of the Bohai Bay Basin (35.8 °C/km) [40]. Compared with some others, the Jiyang Depression has a relatively high geothermal gradient, and according to the standard of geothermal zoning in Chinese oil and gas basins [41], the Jiyang Depression is a “hot basin”. The reason for the formation of the hot basin is related to the deep faults in the depression.

From the statistical results of the variation range and average value of the geothermal gradient in the four main depressions of the Jiyang Depression (Table 3), it can be seen

that in the longitudinal direction, the geothermal gradient decreases with increasing depth. As for the entire region, the Zhanhua Sag has the largest change in geothermal gradient in various depth ranges, with the highest gradient value, followed by the Dongying Sag, and the Huimin Sag has the lowest geothermal gradient. Laterally, the average geothermal gradient of each depression is different. Among them, the Zhanhua Depression has the highest average geothermal gradient of 36.1 °C/km, which is greater than the average of the entire region. The average geothermal gradient in the Huimin Sag is the lowest at 34.6 °C/km, which is smaller than the average in the entire region. The geothermal gradients in the Dongying and Chezhen Depressions are basically consistent with the average value of the entire region. As a whole, the overall difference is small although the geothermal gradients in each depression are different [42].

**Table 3.** Statistical list of current geothermal gradients at different depths in each structural unit of the Jiyang Depression [42].

Depth Range	Geothermal Gradient (°C/km)									
	Jiyang Depression		Dongying Depression		Huimin Depression		Zhanhua Depression		Chezhen Depression	
	Average Value	Range	Average Value	Range	Average Value	Range	Average Value	Range	Average Value	
0–2 km	36.9	25.5–45.0	36.5	27.9–43.2	34.9	30.1–44.9	37.6	29.5–42.5	36.5	
2–3 km	35.2	29.6–44.0	35.3	29.0–39.5	34.4	24.2–44.7	35.5	28.1–42.0	35.2	
3–4 km	30	29.9–33.1	33.8	21.1–38.4	30	20.9–44.8	34.5	27.1–38.0	33.1	
>4 km	29	<29.0	<29.0	<26.0	<26.0	<32	<32	<28.0	<28.0	
Total average	35.5	35.5	35.5	34.6	34.6	36.1	36.1	35.4	35.4	

It can be seen from Figure 13 that the geothermal gradient distribution in the Jiyang Depression is mainly controlled by the convex and concave basin structural pattern, and is distributed in an alternating pattern of high and low values. The high-value areas are distributed in basement uplifts and low uplifts or slopes, such as Yihezhuang, Chenjiazhuang, Binxian, Qingcheng, Guangrao and other uplifts and isolated island areas. The geothermal gradient is generally as high as 39.0 °C/km or more. The Kendong buried mountainous area has the highest value which is greater than 40.0 °C/km. The low gradient distribution area corresponds to the sag area, and the low-value center is basically consistent with the depocenter of the sag. The geothermal gradient is generally less than 34.0 °C/km, and the lowest point is located in the Linyi depression of the Huimin Sag, below 32.0 °C/km. In addition, some areas with relatively high geothermal gradients in the Jiyang Depression are basically consistent with the distribution of Cenozoic volcanic rocks [43].

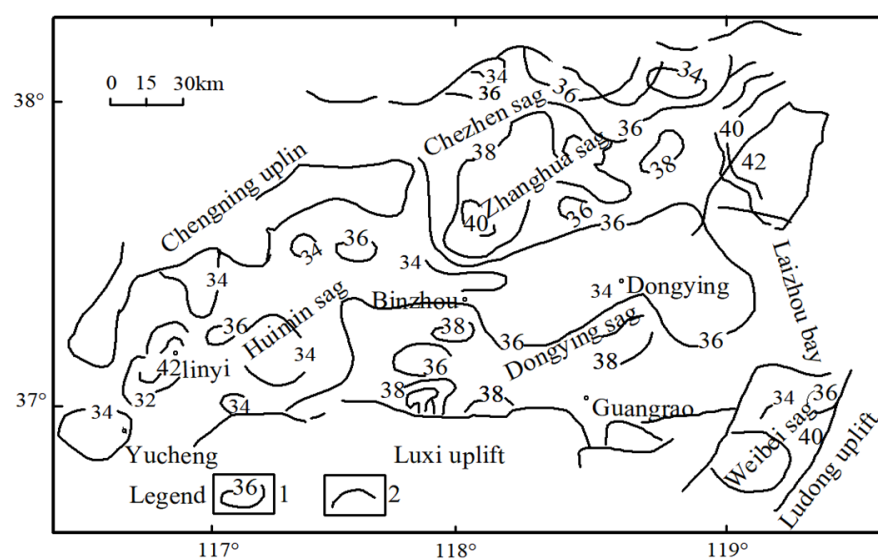


**Figure 13.** Geothermal gradient contour map of Jiyang Depression [42]. 1 Geothermal gradient contour (°C/km); 2 Basin boundary.

The lateral variation characteristics of the geothermal gradient in the Jiyang Depression are related to the basement depth and the distribution of volcanic rocks. The geothermal gradient is high in the raised areas with a shallow basement and Cenozoic volcanic rock distribution areas, whereas the geothermal gradient is relatively low in the depression areas with a large basement depth. The basement depth in the basin area and the distribution of bulges and depressions in the basin are controlled by the Cenozoic lithospheric extension process, and the distribution of volcanic rocks is also related to this period of the lithospheric extension process. The geothermal gradient characteristics of the Jiyang Depression are determined by Cenozoic tectonic-volcanic events. Since the Cenozoic, especially in the Early Tertiary, tectonic-thermal events in the Jiyang Depression have been very frequent, which is the main reason for the high geothermal gradient. In the late Tertiary, tectonic activities in the entire region became consistent and gradually weakened, and the difference in subsidence in each depression decreased, changing from differential subsidence to overall subsidence. Therefore, there are certain differences in geothermal gradients among various unit areas in the Jiyang Depression, and the small differences not only reflect the differences in tectonic activity of the different tectonic units but also reflect the consistency of tectonic conditions in the entire region [42].

#### 4.1.3. Characteristics of the Electric Field

Zhang Jihong and other scholars have studied the electrical structure of the Yishu Fault in the eastern Jiyang Depression. From the interpretation of the Luxi Uplift, the resistivity of the lower part of the Luxi Uplift is generally relatively high, and there is no high conductivity layer in the crust. Its resistivity is related to more mafic or granulite formations [44]. We collected and sorted out the electrical logging data of three wells near the measurement area (Well Fanshen 1, Well Gaoshen 1 and Well Lin 28). Among them, Well Lin 28 is the deepest and the depth of the Shanxi Formation reaches 4500 m. Electrical logging curves show that there are vertical differences in resistivity in this area, with an overall “high-low-high” change from the Quaternary Plain Formation (Qp) to the Lower Paleozoic Ordovician Badou Formation (O2b).

#### 4.2. Solution of Wide Field Electromagnetic Detection

According to the geological task requirements and combined with the surface conditions of the work area, the design is carried out according to the 200 m point spacing of the WFEM method and the 2 km point spacing of the magnetotelluric sounding method. At the same time, a WFEM method of 100 m point spacing was applied to refine the main fault zones of the penetration survey line, and a 1 km distance electromagnetic sounding method was used to refine the buried hill areas such as Wangpan Town Buried Hill and Bangu 4. Since seismic work has been conducted in this area, during the process of the survey line design, the line numbers and point numbers of the WFEM survey points were fully consistent with the earthquake numbers, and the survey lines completely covered the seismic survey lines.

We designed and completed two measuring lines of the WFEM method (as shown in Figure 14) with 1049 measuring points. Among them, line WPZ65.8 has six transmitting field sources with a total of 294 measuring points (as shown in Figure 15) whereas the WPZ534.2 line has 19 transmitting field sources with a total of 755 measuring points, and the sending and receiving distance is about three times the detection depth in the field source layout. There are two measuring lines of the magnetotelluric sounding method with 111 measuring points, and the measuring line length is 150.3 km, including two magnetotelluric sounding points next to the drilling well (Table 4).

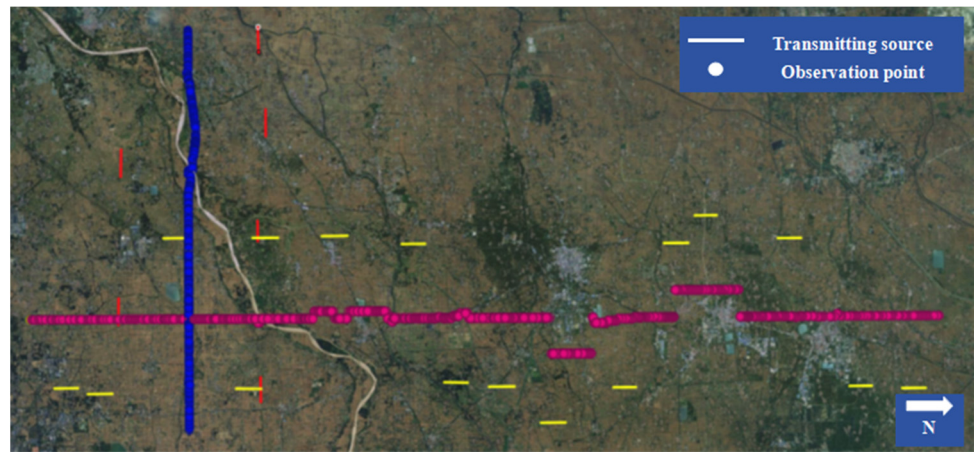


**Figure 14.** Diagram of the layout of Jiyang wide field electromagnetic survey line (Horizontal lines represent the WFEM's transmission field sources, and circles indicate measurement points).

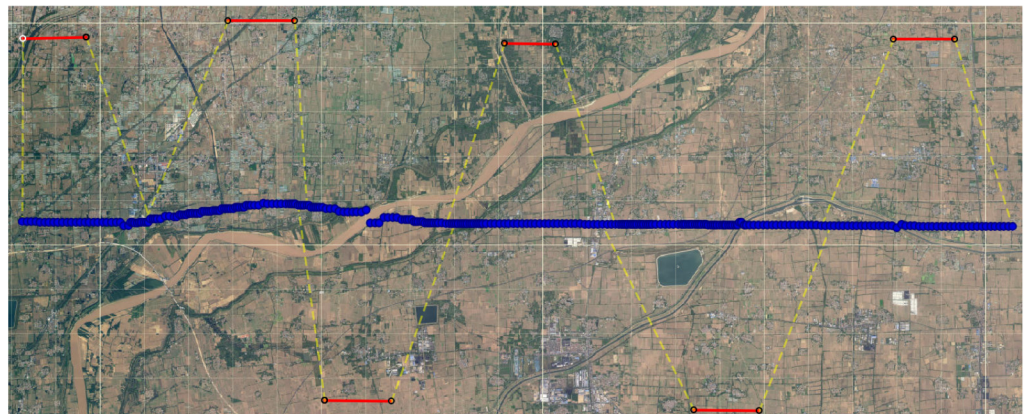


**Figure 15.** Diagram of the field source of the Wide field electromagnetic line WPZ65.8 and the layout of measurement line (Yellow dashed lines indicate the coverage area of the field source, red solid lines represent the transmission field sources, and blue dots denote measurement points).

**Table 4.** Workload of electrical exploration and design in Wangpan Town.

Line Number	Measuring Line Length	WFEM		MT	
		Measuring Point	Checking Point	Measuring Point	Checking Point
WPZ65.8	44.3	294	12	45	3
WPZ534.2	106.0	755	27	66	3
Well-side sounding	-	-	-	2	-
Summation	150.3	1049	39	113	6

### 4.3. Data Processing and Result Analysis

#### 4.3.1. Data Processing

Figure 16 depicts the original WFEM apparent resistivity profiles of line WPZ65.8 and line WPZ534.2 (straightening is used to calculate the distances for measuring points). The apparent resistivity characteristics of the high-frequency band and low-frequency band in the figure show high values. Generally speaking, it conforms to the “high-low-high” characteristics of the stratigraphy in the area. Since this area is relatively flat and the electrical distribution is relatively layered, the apparent resistivity at the junction of multiple field source measurement lines is not much different, and the overall apparent resistivity shape remains consistent, so a hard splicing method is adopted.

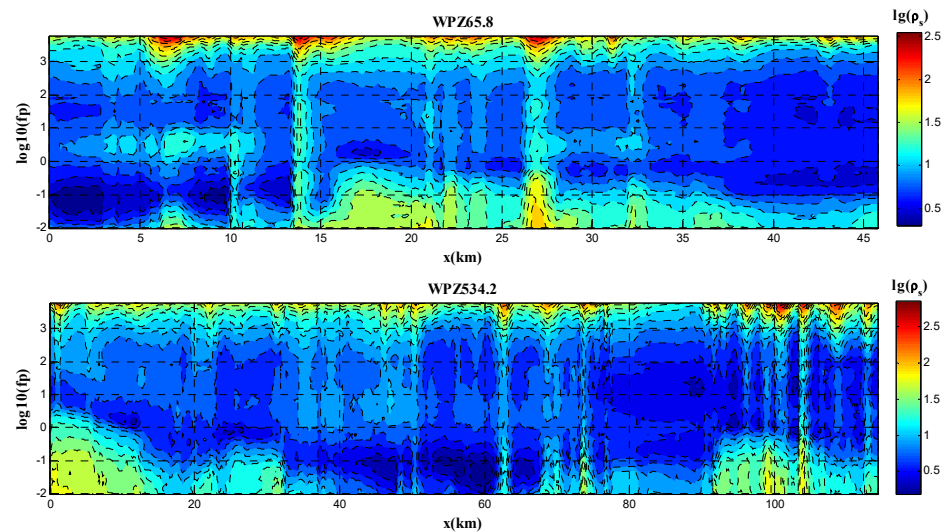


**Figure 16.** Original apparent resistivity profile of wide field electromagnetic survey line.

The original data are less affected by static effects. In order to retain the small structures in the original data as much as possible, horizontal filtering is performed along the data processing to increase the smoothness of the data and improve the fitting degree of the data inversion. Using the passive inversion algorithm with terrain (TM polarization mode of 2D MT), the initial fitting error of the line WPZ534.2 is 77.8%, taking the 20  $\Omega$ m uniform half-space model as the initial model. After six iterative inversions, the final fitting error is 9.59%. The initial fitting error of the line WPZ65.8 is 71.6%. After six iterations, the final fitting error is 12.9%.

Figure 17 shows the 3D inversion imaging results of the two Jiyang WFEM survey lines. It can be seen from the figure that the inversion results of survey line WPZ65.8 and survey line WPZ534.2 are highly consistent at the intersection. This proves that the underground structure in this area is relatively one-dimensional is less affected by the field source effects, and the inversion results are reliable.

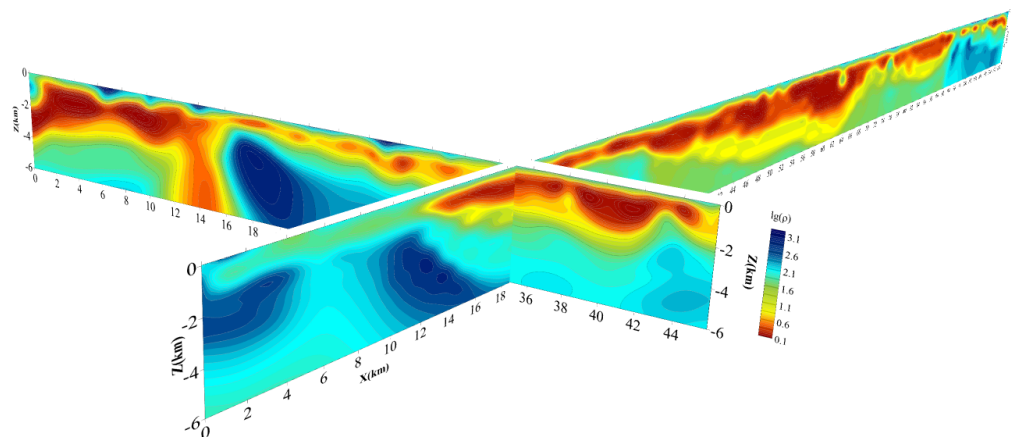


**Figure 17.** The 3D imaging results of two wide field electromagnetic survey lines.

#### 4.3.2. Analysis of the WFEM Detection Results of the Survey Line WPZ65.8

Figure 18 presents the wide field electromagnetic imaging results and interpretation comparison chart of the line PZ65.8 with an inversion profile depth of 6000 m. Three normal faults (F1, F2 and F3) can be identified laterally, dividing the strata into a structural pattern of one uplift (Wangpanzhen buried hill) and two depressions (Jiyang Graben, Huagou depression). They are also important in the thermal fault of Jiyang Depression. From top to bottom, they are the Quaternary, Neogene (Q + N), and Paleogene Series (E), Jurassic and Cretaceous (K + J) and Carboniferous (C). The first layer of the Quaternary

and Neogene systems is stably developed, with a thickness of about 800–1100 m, and a generally low resistivity of about 1–5  $\Omega\text{m}$ . On the surface, there is a widely distributed and relatively gentle layer of medium-high resistivity, which is the intrusion of Neogene igneous rocks with a resistivity between 500 and 1500  $\Omega\text{m}$ . The second layer is the Paleogene (E) with a relatively low resistivity. There are two secondary depressions around 0–12 km and 15–45 km, with a resistivity of around 1–5  $\Omega\text{m}$ . The third layer is the Jurassic and Cretaceous (K + J) strata with a medium resistivity of about 50–100  $\Omega\text{m}$ ; the strata of the Carboniferous and below are of a high resistivity greater than 500  $\Omega\text{m}$ . Compared with wide-field electromagnetic, magnetotelluric and seismic profiles, the results of the WFEM exploration are closer to those of the seismic profile, with consistent overall stratigraphy and structure but richer in details with higher reliability.

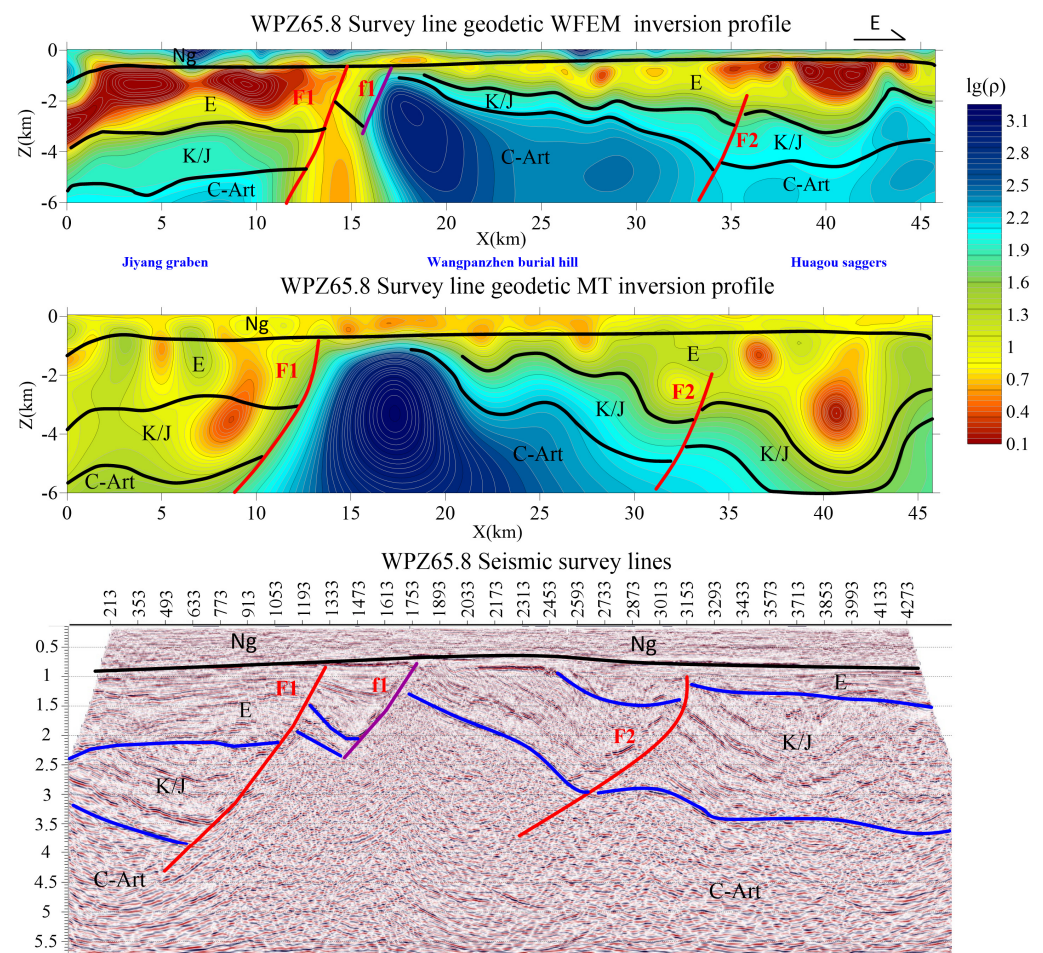


**Figure 18.** Imaging results and interpretation comparison chart of the survey line WPZ65.8.

#### 4.3.3. Analysis of the WFEM Detection Results of the Survey Line WPZ534.2

Figure 19 illustrates that the WFEM imaging results and interpretation comparison chart of line WPZ534.2 are in good agreement with those of the survey line WPZ65.8. Seven faults can be identified laterally, among which F1, F2, F3, and F4 are deep faults that control the depression. The four faults divide the depression into four uplifts (Luxi, Qingcheng, Linfanjia and Wudi). The structural pattern of the three depressions (Huagou, Lizezhen and Yangxin) is also an important thermal control fault in the depression. From top to bottom, they are the Quaternary and Neogene (Q + N), Paleogene (E), Jurassic and Cretaceous (K + J) and Carboniferous (C). The first layer of Quaternary and Neogene systems are stable in development, and there is a widely distributed and relatively gentle layer of medium-high resistance strata on the surface, indicating that the Neogene systems in the Wangpan Town area are stable in development. Luxi uplift lacks the Jurassic and Cretaceous (K + J),

and the low-resistivity of the Tertiary system directly enters the high-resistivity strata with a resistivity greater than  $500 \Omega\text{m}$ . The strata in the depressions of Huagou, Lize Town and Yangxin are all relatively well-developed. The second layer is the Paleogene (E) with a relatively low apparent resistivity. The stratum as a whole tilts to the north with a resistivity of  $5\text{--}12 \Omega\text{m}$ . The third layer is the Jurassic and Cretaceous (K + J) strata with a medium resistivity of about  $50\text{--}100 \Omega\text{m}$ ; the fourth layer, the Carboniferous and below strata, has a high resistivity greater than  $500 \Omega\text{m}$ .

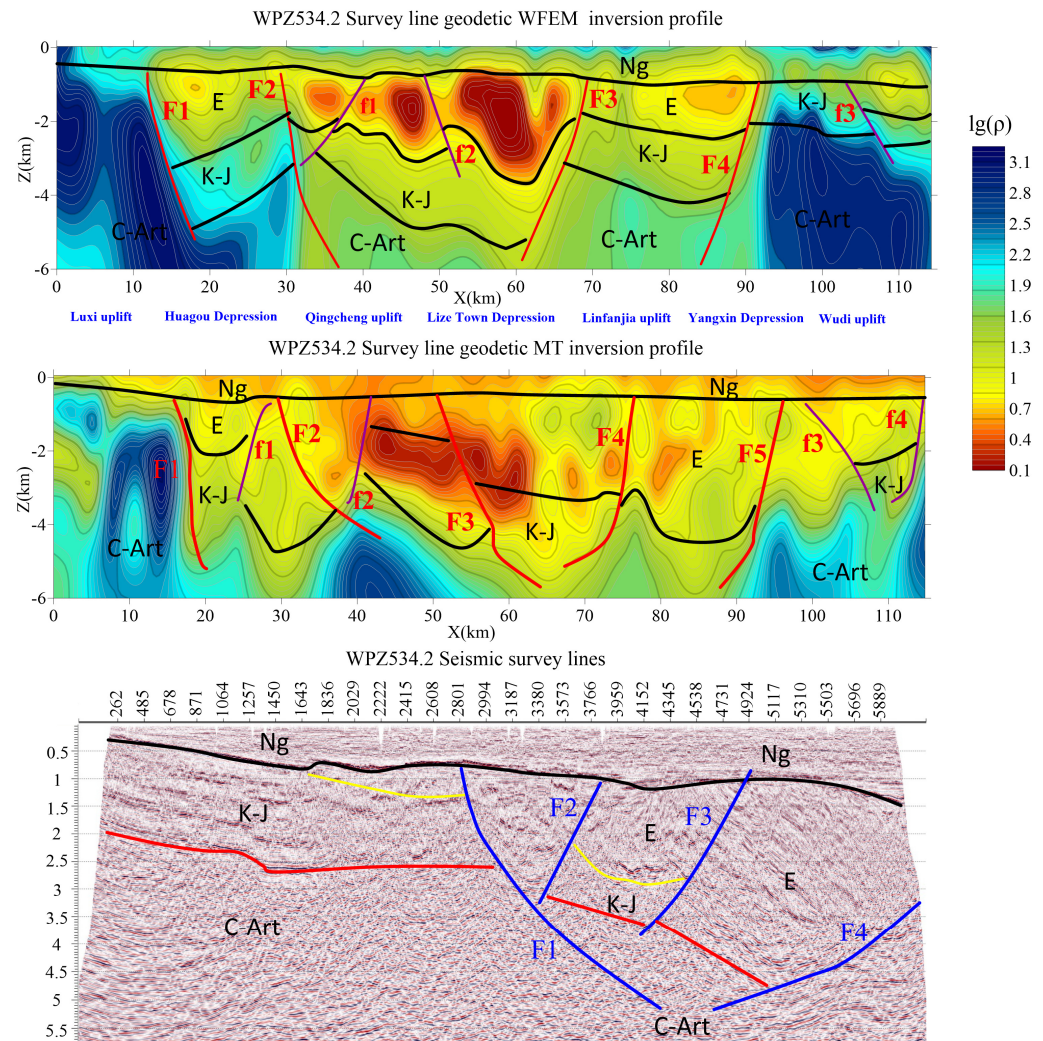


Figure 19. Imaging results and interpretation comparison chart of the survey line WPZ534.2.

## 5. Conclusions

- (1) The numerical simulation results of the WFEM method revealed that for a hydrothermal geothermal resource target, detection is feasible when the thickness-to-depth ratio exceeds 1%, and the ratio of the thickness-to-depth ratio to the resistivity contrast ratio (the ratio of the target's resistivity to the background resistivity) exceeds 10%. For hot dry rock geothermal resource targets, detection is feasible when the thickness-to-depth ratio exceeds 5%, and the product of the thickness-to-depth ratio and the resistivity contrast ratio is approximately greater than 25%.
- (2) It is difficult to detect the geothermal resources in the middle and deep layers. The WFEM method also faces a lot of difficulties in field source deployment, data acquisition, data processing and inversion algorithms. So, it is necessary to choose a suitable solution in fieldwork to improve the reliability of the detection results.

- (3) Human interference is serious in geothermal energy detection in the middle and deep layers of the Jiyang Depression. The WFEM method has obtained raw data with a relatively high signal-to-noise ratio quality. The overall apparent resistivity profile is consistent with the changing trend of formation lithology, and the uplift and depression divisions are in good agreement with the actual geological conditions. The 2D WFEM inversion results can make mutual verification and reference with the magnetotelluric profile and seismic profile. On the premise of maintaining the consistency of the overall large structure, the shallow depth resolution of the WFEM inversion profile is higher with richer details than the others, which makes up for the weak links in the seismic profile.
- (4) According to the uplift and pattern of the depression and the distribution of the main heat-controlling structures, the Huagou depression is a mid-rise one, which has a well-developed caprock and a shallowly basement, sandwiched by two heat-controlling faults F1 and F2, possessing a high potential of both hydrothermal and hot dry rock geothermal resources, whereas the Linfanjia Uplift is an uplift in a depression, sandwiched by two deep thermal conductive faults F3 and F4, also having a high potential of deep geothermal resources.
- (5) WFEM methods are efficacious for probing medium to deep geothermal energy resources. However, practical applications encounter numerous challenges. It is recommended to employ a multiplicity of geophysical exploration techniques to enhance the reliability of detection outcomes.

**Author Contributions:** Methodology, G.F., Z.L. and Q.Z.; Software, X.C., C.L. and J.L.; Formal analysis, Q.J.; Investigation, T.G., Q.J., Y.Y., X.C., C.L. and J.L.; Writing—original draft, Z.L.; Writing—review & editing, G.F. and Q.Z.; Visualization, T.G. and Y.Y. All authors have read and agreed to the published version of the manuscript.

**Funding:** This work is sponsored by the Jiangsu Province Carbon Peak Carbon Neutral Technology Innovation Project in China (BE2022034), and the Guangdong Provincial Marine Economy Special Project (No. GDNRC [2021]57), and the Key Research and Development Program in Yunnan Province of China (No. 202302AF080001), (No. 202302AC080003), (No. 202303AA080006), and the Shenzhen Municipal Science and Technology Innovation Committee (No. JCYJ20220818103010021), and Natural Science Foundation Project in Guangxi of China (No. 2018GXNSFAA050070, No. GKAD19110058, and GKN2201K004), and the Sinopec Science and Technology Research Project (No. P21079-3 and No. P22090).

**Data Availability Statement:** The original contributions presented in the study are included in the article, further inquiries can be directed to the corresponding authors.

**Conflicts of Interest:** Author Zhuqiang Li, Tao Guo, Yonghong Yang and Xueguo Chen were employed by the Shengli Oilfield Company, SINOPEC; Author Chuang Lei was employed by the Sinopec Geophysical Corporation Geographical & Geological Exploration Branch. The remaining authors declare that the research was conducted in the absence of any commercial or financial relationships that could be construed as a potential conflict of interest.

## References

1. Soltani, M.; Kashkooli, F.M.; Dehghani-Sanij, A.R.; Nokhosteen, A.; Ahmadi-Joughi, A.; Gharali, K.; Mahbaz, S.B.; Dusseault, M.B. A comprehensive review of geothermal energy evolution and development. *Int. J. Green Energy* **2019**, *16*, 971–1009. [[CrossRef](#)]
2. Dhar, A.; Naeth, M.A.; Jennings, P.D.; Gamal El-Din, M. Geothermal energy resources: Potential environmental impact and land reclamation. *Environ. Rev.* **2020**, *28*, 415–427. [[CrossRef](#)]
3. Pang, Z.H.; Luo, J.; Cheng, Y.Z.; Duan, Z.F.; Tian, J.; Kong, Y.L.; Li, Y.M.; Hu, S.B.; Wang, J.Y. Evaluation of geological conditions for the development of deep geothermal energy in China. *Earth Sci. Front.* **2020**, *27*, 134–151.
4. Wang, G.L.; Zhang, W.; Ma, F.; Lin, W.J.; Liang, J.Y.; Zhun, X. Overview on hydrothermal and hot dry rock researches in China. *China Geol.* **2018**, *1*, 273–285. [[CrossRef](#)]
5. Wang, G.L.; Lin, W.J.; Liu, F.; Gan, H.N.; Wang, S.Q.; Yue, G.F.; Long, X.T.; Liu, Y.G. Theory and survey practice of deep heat accumulation in geothermal system and exploration practice. *Acta Geol. Sin.* **2023**, *97*, 639–660.
6. Barbier, E. Geothermal energy technology and current status: An overview. *Renew. Sustain. Energy Rev.* **2002**, *6*, 3–65. [[CrossRef](#)]

7. Kana, J.D.; Djongyang, N.; Raïdandi, D.; Nouck, P.N.; Dadjé, A. A review of geophysical methods for geothermal exploration. *Renew. Sustain. Energy Rev.* **2015**, *44*, 87–95. [[CrossRef](#)]
8. Zhang, S.Q.; Li, X.F.; Song, J.; Wen, D.G.; Li, Z.W.; Li, D.P.; Cheng, Z.P.; Fu, L.; Zhang, L.Y.; Feng, Q.D.; et al. Analysis on geophysical evidence for existence of partial melting layer in crust and regional heat source mechanism for hot dry rock resources of Gonghe Basin. *J. Earth Sci.* **2021**, *46*, 1416.
9. Van der Meer, F.; Hecker, C.; van Ruitenbeek, F.; van der Werff, H.; de Wijkerslooth, C.; Wechsler, C. Geologic remote sensing for geothermal exploration: A review. *Int. J. Appl. Earth Obs. Geoinf.* **2014**, *33*, 255–269. [[CrossRef](#)]
10. Cagniard, L. Basic theory of the magnetotelluric method of geophysical prospecting. *Geophysics* **1953**, *18*, 605–635. [[CrossRef](#)]
11. Marwan; Yanis, M.; Idroes, R.; Ismail, N. 2D inversion and static shift of MT and TEM data for imaging the geothermal resources of Seulawah Agam Volcano, Indonesia. *Int. J. Geomate.* **2019**, *17*, 173–180. [[CrossRef](#)]
12. Spichak, V.; Manzella, A. Electromagnetic sounding of geothermal zones. *J. Appl. Geophys.* **2009**, *68*, 459–478. [[CrossRef](#)]
13. Jegen, M.D.; Hobbs, R.W.; Tarits, P.; Chave, A. Joint inversion of marine magnetotelluric and gravity data incorporating seismic constraints. *Earth Planet Sci. Lett.* **2009**, *282*, 47–55. [[CrossRef](#)]
14. Muñoz, G. Exploring for Geothermal Resources with Electromagnetic Methods. *Surv. Geophys.* **2014**, *35*, 101–122. [[CrossRef](#)]
15. Ren, W.Q.; Ren, Z.Y.; Xue, G.Q.; Chen, W.Y.; Zhao, P.; Liu, J.L. Three-dimensional audio magnetotelluric imaging of the Yangyi geothermal field in Tibet, China. *J. Appl. Geophys.* **2023**, *211*, 104966. [[CrossRef](#)]
16. Cheng, Z.P.; Lei, M.; Li, S.; Lian, S.; Wei, Q. Research on time-frequency electromagnetic method detection of deep karst thermal reservoir and prediction of favorable area in Dongli Lake of Tianjin. *N. Chin. Geol.* **2023**, *46*, 1–8.
17. Kouadio, K.L.; Xu, Y.X.; Liu, C.M.; Boukhalifa, Z. Two-dimensional inversion of CSAMT data and three-dimensional geological mapping for groundwater exploration in Tongkeng Area, Hunan Province, China. *J. Appl. Geophys.* **2020**, *183*, 104204. [[CrossRef](#)]
18. Wang, J.C.; Zhao, Z.G.; Gao, S.Y.; Luo, C.G.; Li, L.; Xu, M.Z.; Li, Y.; Yuan, G.J. Application of a comprehensive geophysical exploration methods in the exploration of geothermal resources in Yueliang, Binhai County. *Geophys. Geochem. Explor.* **2023**, *47*, 321–330.
19. Wu, G.J.; Hu, X.Y.; Huo, G.P.; Zhou, X.C. Geophysical Exploration for geothermal resources: An Application of MT and CSAMT in Jiangxia, Wuhan, China. *J. Earth Sci.* **2012**, *23*, 757–767. [[CrossRef](#)]
20. Hu, Y.F.; Li, D.Q.; Yuan, B.; Suo, G.Y.; Liu, Z.J. Application of pseudo-random frequency domain electromagnetic method in mining areas with strong interferences. *Trans. Nonferrous Met. Soc. China* **2020**, *30*, 774–788. [[CrossRef](#)]
21. Zhu, Y.Q.; Li, D.Q.; Hu, Y.F.; Zhang, X.; Li, F.; Ma, F.; Wang, G.L. Deep structure of the Rongcheng geothermal field, Xiongan New Area: Constraints from resistivity data and boreholes. *Geothermics* **2023**, *114*, 102776. [[CrossRef](#)]
22. Lüschen, E.; Wolfram, M.; Fritzer, T.; Dussel, M.; Thomas, R.; Schulz, R. 3D seismic survey explores geothermal targets for reservoir characterization at Unterhaching, Munich, Germany. *Geothermics* **2014**, *50*, 167–179. [[CrossRef](#)]
23. Pussak, M.; Bauer, K.; Stiller, M.; Bujakowski, W. Improved 3D seismic attribute mapping by CRS stacking instead of NMO stacking: Application to a geothermal reservoir in the Polish Basin. *J. Appl. Geophys.* **2014**, *103*, 186–198. [[CrossRef](#)]
24. Asrillah, A.; Abdullah, A.; Bauer, K.; Norden, B.; Krawczyk, C.M. Fracture characterisation using 3-D seismic reflection data for advanced deep geothermal exploration in the NE German Basin. *Geothermics* **2024**, *116*, 102833. [[CrossRef](#)]
25. Represas, P.; Monteiro, S.F.A.; Ribeiro, J.; Ribeiro, J.A.; Almeida, E.P.; Gonçalves, R.; Moreira, M.; Mendes-Victor, L.M. Interpretation of gravity data to delineate structural features connected to low-temperature geothermal resources at Northeastern Portugal. *J. Appl. Geophys.* **2013**, *92*, 30–38. [[CrossRef](#)]
26. Witter, J.B.; Siler, D.L.; Faulds, J.E.; Hinz, N.H. 3D geophysical inversion modeling of gravity data to test the 3D geologic model of the Bradys geothermal area, Nevada, USA. *Geotherm. Energy* **2016**, *4*, 14. [[CrossRef](#)]
27. Pocasangre, C.; Fujimitsu, Y.; Nishijima, J. Interpretation of gravity data to delineate the geothermal reservoir extent and assess the geothermal resource from low-temperature fluids in the Municipality of Isa, Southern Kyushu, Japan. *Geothermics* **2020**, *83*, 101735. [[CrossRef](#)]
28. He, J.S. Combined Application of Wide-Field Electromagnetic Method and Flow Field Fitting Method for High-Resolution Exploration: A Case Study of the Anjialing No.1 Coal Mine. *Engineering* **2018**, *4*, 188–205. [[CrossRef](#)]
29. Tang, J.T.; He, J.S. *The Method of CSAMT and Its Application*; Central South University Press: Changsha, China, 2005. (In Chinese)
30. Zhang, X.; Li, D.Q.; Li, J.; Liu, B.; Jiang, Q.Y.; Wang, J.H. Signal-Noise Identification for Wide Field Electromagnetic Method Data Using Multi-Domain Features and IGWO-SVM. *Fractal Fract.* **2022**, *6*, 80. [[CrossRef](#)]
31. Xiao, J.Y. *Application of Orthogonal Source Wide-Field Electromagnetic Method in the Detection of Water-Rich Area of Coal Mine*; Central South University: Changsha, China, 2021. (In Chinese)
32. Zhang, B.M.; Jiang, Q.Y.; Mo, D.; Xiao, L.Y. A novel method for handling gross errors in electromagnetic prospecting data. *Chin. J. Geophys.* **2015**, *58*, 2087–2102.
33. Zhou, C.; Tang, J.T.; Pang, C.; Hu, S.G. A theory and simulation study on the space-time array hybrid source electromagnetic method. *Chin. J. Geophys.* **2019**, *62*, 3827–3842.
34. Yang, Y.; He, J.S.; Li, D.Q. Energy distribution and effective components analysis of 2n sequence pseudo-random signal. *Trans. Nonferrous Met. Soc. China* **2021**, *31*, 2102–2115. [[CrossRef](#)]
35. Ye, T.; Chen, X.B.; Yan, L.J. Reined techniques for data processing and two-dimensional inversion in magnetotelluric (III): Using the Impressing Method to construct starting model of 2D magnetotelluric inversion. *Chin. J. Geophys.* **2013**, *56*, 3596–3606.

36. Cui, Y.A.; Zhang, L.J.; Zhu, X.X.; Liu, J.X.; Guo, Z.W. Inversion for magnetotelluric data using the particle swarm optimization and regularized least squares. *J. Appl. Geophys.* **2020**, *181*, 104156. [[CrossRef](#)]
37. Niu, Z.C.; Wang, Y.S.; Wang, X.J.; Zhang, X.J.; Wang, X.H.; Han, D.M.; Liu, X.; Wang, R.; Wang, J. Hydrocarbon Generation Potential of Pre-Paleogene Source Rocks in the Jiyang Depression. *Geol. J. China Univer.* **2022**, *28*, 73–85.
38. Cheng, B.H.; Xu, L.; Xiang, X.Y.; Mu, X. Present-day geothermal field and thermal history of the Zhanhuadong Block, Jiyang depression. *Chin. J. Geophys.* **2001**, *44*, 238–244.
39. Wang, L.S.; Liu, S.W.; Xiao, W.Y.; Li, C.; Li, H.; Guo, S.P.; Liu, B.; Luo, Y.H.; Cai, D.S. Characteristics of geothermal flux distribution in the Bohai Basin. *Chin. Sci. B* **2002**, 151–155.
40. Qiu, N.S.; Zuo, Y.H.; Zhou, X.H.; Li, C.C. Geothermal regime of the Bohai Offshore Area, Bohai Bay Basin, North China. *Energy Explor. Exploit.* **2010**, *28*, 327–350. [[CrossRef](#)]
41. Wu, S.C. A systematic study of the Chinese petroliferous basins. *Acta Pet. Sin.* **1993**, *14*, 20–34.
42. Gong, Y.L.; Wang, L.S.; Liu, S.W.; Guo, L.Z.; Cai, J.G. Distribution characteristics of geotemperature field in Jiyang depression, Shandong, north China. *Chin. J. Geophys.* **2003**, *46*, 652–658.
43. Zong, G.H. *Study on Tectonic Model and Hydrocarbon Accumulation in Jiyang Depression*; Nanjing University: Nanjing, China, 1997. (In Chinese)
44. Zhang, J.H.; Zhao, G.Z.; Xiao, Q.B.; Tang, J. Analysis of electric structure of the central Tan-Lu fault zone (Yi-Shu fault zone, 36°N) and seismogenic condition. *Chin. J. Geophys.* **2010**, *53*, 605–611.

**Disclaimer/Publisher’s Note:** The statements, opinions and data contained in all publications are solely those of the individual author(s) and contributor(s) and not of MDPI and/or the editor(s). MDPI and/or the editor(s) disclaim responsibility for any injury to people or property resulting from any ideas, methods, instructions or products referred to in the content.